Chinese Chemical Letters 35 (2024) 108752

Contents lists available at ScienceDirect

Chinese Chemical Letters

journal homepage: www.elsevier.com/locate/cclet

Multifunctional nano-herb based on tumor microenvironment for enhanced tumor therapy of gambogic acid

Fengyun Li[a,1], Zerong Pei[a,1], Shuting Chen[a], Gen li[a], Mengyang Liu[c], Liqin Ding[c], Jingbo Liu[b,*], Feng Qiu[a,*]

[a] School of Chinese Materia Medica, Tianjin University of Traditional Chinese Medicine, Tianjin 301617, China
[b] College of Horticulture and Landscape Architecture, Tianjin Agricultural University, Tianjin 300384, China
[c] State Key Laboratory of Component-based Chinese Medicine, Tianjin University of Traditional Chinese Medicine, Tianjin 301617, China

ARTICLE INFO

Article history:
Received 28 March 2023
Revised 20 June 2023
Accepted 28 June 2023
Available online 1 July 2023

Keywords:
Tumor microenvironment
Microgels
Gambogic acid
Dual-active targeting
Triple environment responsiveness
Silver nanoclusters

ABSTRACT

Multifunctional drug delivery systems (DDSs) have shown great prospects in overcoming the heterogeneous barrier of delivery drugs to the complex tumor microenvironment (TME). In this study, multifunctional AS/Ge-pNAB microgels with dual-active targeting, triple environment responsiveness, and fluorescence imaging capability were prepared through a straightforward procedure. This was aimed to improve the antitumor therapeutic application of gambogic acid (GA) based on the biological characteristics of TME. The microgels have a uniform double-layer structure with aptamer in the outer layer which helps in recognizing receptors on the tumor cells. The GA loaded nano-herb exhibited environment-responsive drug release profiles under acidic pH, reductant and high temperature. The nano-herb significantly improved the accumulation of GA in tumor sites through the synergistic combination of the enhanced permeability and retention effect and dual-ligand mediated internalization. Then, it accelerated intracellular drug release and killed tumor cells. Therefore, the nano-herb had specific therapeutic effects on the tumor *in vitro* and *in vivo* as they remarkably inhibited tumor growth while depicting optimal biosafety and lower levels of off-target toxicity. Overall, these findings demonstrate the great potential of the multifunctional AS/Ge-pNAB microgels for precisely targeted GA delivery and open a new avenue for the facile preparation of multifunctional DDSs.

Chemotherapy is still the most commonly used treatment for many cancers [1]. In comparison to surgery and radiotherapy that can only target local tumors, chemotherapy is more suitable for some patients with systemic spread-prone tumors and advanced metastasized tumors [2,3]. Herbal medicines exhibit broad-spectrum therapeutic potentials, especially in antitumor applications [4]. Compared with traditional chemotherapeutic drugs, herbal medicines have many unique advantages in terms of antitumor activities such as multi-target, multi-level, coordinated intervention effects, and more [5,6].

Gambogic acid (GA), the main effective moiety extracted from the *Garcinia hanburyi* tree, is a promising multi-target antitumor drug with significant cytotoxic activity against various tumors [7,8]. Nevertheless, the clinical application of GA has been limited due to its instability, short half-life, poor solubility and systemic toxicity [9,10]. In order to overcome the issues with traditional dosage forms, nano-drug delivery systems (nano-DDSs) can be used to improve drug targeting, stability, bioavailability, and control drug release [11–14]. At present, a small amount of nano-DDSs have been investigated to increase the druggability of GA, including liposomes [15], micelles [16], core-shell nanoparticles [17], and hydrogels [18]. However, these nano-DDSs often have low drug loading capacity and poor stability, especially their single function, which can not cope with the complex tumor microenvironment (TME) *in vivo,* resulting in low delivery efficiency and no obvious improvement in drug efficacy. Therefore, developing new multifunctional nano-DDSs based on the biological characteristics of the TME will be an effective way to further improve the antitumor efficacy of GA.

An increasing set of studies have indicated that TME plays an essential role in determining the fate of nano-drug delivery systems *in vivo* [19]. The drug delivery efficiency is largely hindered by tumor heterogeneity [20], including abnormal vasculature, rigid

* Corresponding authors.
E-mail addresses: liujingbo0626@163.com (J. Liu), fengqiu20070118@163.com (F. Qiu).
[1] These authors contributed equally to this work.

https://doi.org/10.1016/j.cclet.2023.108752
1001-8417/

ECM, immune suppression, acidic pH, and excessive glutathione, *etc*. The commonly used and effective ways to overcome the heterogeneous barrier of the TME include TME modulation [21], actively targeting TME [22], and TME-responsive drug delivery [23]. To sum up, multifunctional nano-DDSs with both the ability of actively targeting and response to TME have shown great potential in delivering antitumor drugs in complex TME [24]. However, to the best of our knowledge, no such reliable multifunctional nano-DDSs have yet entered into clinical trials. This can be likely associated with their complicated manufacturing process, high cost, toxicity, and infeasible large-scale production for routine patient treatment. It is thus vital that a simple approach to the preparation of multifunctional nano-DDSs be established to cater to the need for patient treatment.

Additionally, the introduction of observable signals into the nano-DDSs, such as magnetic resonance signal [25], photoacoustic signal [26] and fluorescence [27] can realize the dynamic monitoring of the drug delivery process and play an important role in guiding the drug delivery process. Nucleic acid-stabilized silver nanoclusters (Ag NCs) are a novel kind of hydrophilic fluorophores [28], which are label-free, low-cost, and have unique luminescence properties, including high biocompatibility, photostability, and low toxicity [29,30]. All these advantages make Ag NCs ideal optical labels for sensors and bioimaging. Therefore, introducing Ag NCs into the nano-DDSs will have unique advantages in guiding drug delivery.

Microgels are cross-linked three-dimensional (3D) polymer networks swollen in water with sizes ranging from tens of nanometers (also called "nanogels") to several micrometers [31]. As compared to other nano-DDSs, microgels usually have good biocompatibility, high aqueous dispersibility, and excellent drug-loading ability [32,33]. They also possess stimuli-response properties enabling them to respond to subtle changes in temperature, pH, redox, enzyme, *etc*., in specific sites. Furthermore, their flexibility and softness render them more effective penetration ability and extended circulating lifetime [34,35]. All the above advantages make microgels ideal systems for intracellular drug delivery. In this study, we developed multifunctional AS/Ge-pNAB microgels with dual active targeting, triple environment responsiveness, and fluorescence imaging capability for the delivery of GA through a facile one-step precipitation polymerization strategy based on the biological characteristics of TME (Scheme 1). The microgels utilizes the dual targeting of nucleic acid aptamer (AS) and galactose (Ge) to specifically recognize the overexpressed nucleolin and asialoglycoprotein receptor (ASGPR) on the surface of liver cancer cells, respectively, to precisely deliver GA to the tumor site. The strong and stable fluorescence of DNA-template Ag NCs makes the microgels image tumor cells specifically. Temperature-sensitive poly-*N*-isopropyl acrylamide (pNIPAM) and pH-responsive polyacrylic acid (pAA) as the building materials, respectively. *N*,*N*′-Bis(acryloyl)cystamine (BAC), which can be cleaved by glutathione, was used as a cross-linking agent to achieve triple environmental responsiveness. The microgel formed with single-ligand or no-ligand were AS-pNAB, Ge-pNAB and pNAB, respectively. The GA-loaded microgels AS/Ge-pNAB@GA, also called nano-herb, have excellent stability with minimal drug leakage under normal physiological environment. Moreover, the reductive and acidic intracellular microenvironment of tumor cells is favorable for drug release at the site of action. Meanwhile, under high temperature (slightly higher than normal physiological temperature), the enhanced hydrophobicity of pNIPAM cause microgels shrinkage and trigger the drug release. The triple-responsive nature of this nano-herb enables controlled localized release of GA at tumor sites. Therefore, this nano-herb with the ability to both target and recognize the TME exhibited enhanced antitumor ability *in vitro* and *in vivo* and reduced the toxic side effects caused by the drug off-target.

First of all, we modified the acrylamide group to galactose to obtain AL-Ge (Fig. S1 in Supporting information), which was then combined with other monomers through a simple one-step precipitation polymerization to obtain microgels. Further, we investigated the fine structure of the microgels after staining with uranyl acetate by using TEM imaging. This showed interesting "hula-hoop"

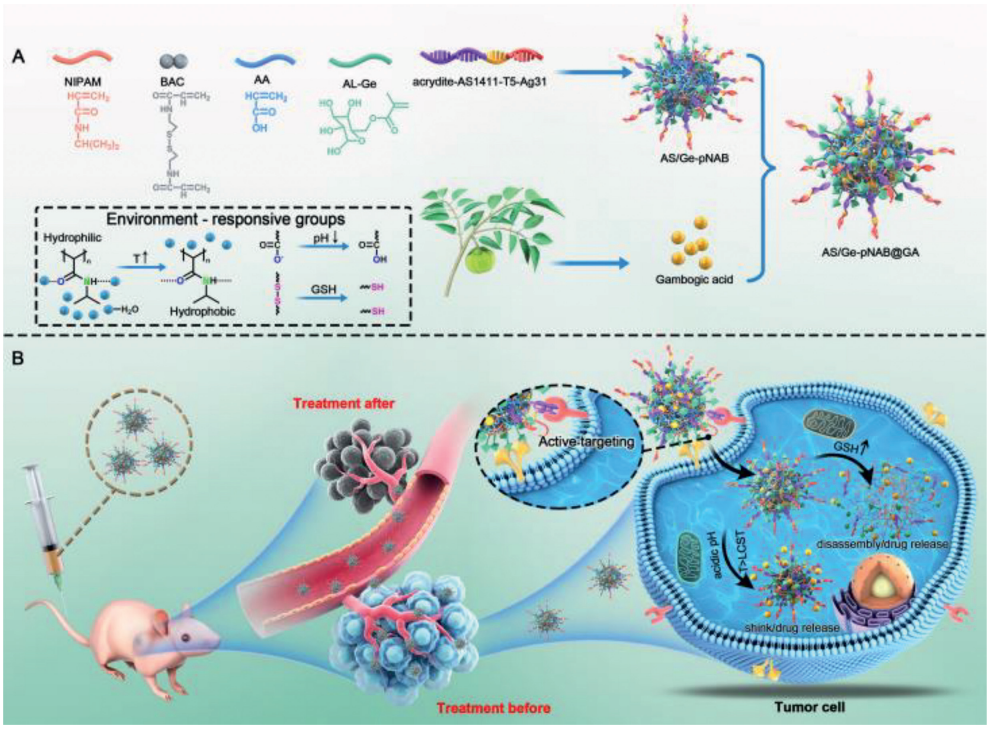

Scheme 1. Schematic overview of the preparation and application of multifunctional nano-herb for precisely targeted delivery of gambogic acid *in vitro* and *in vivo*.

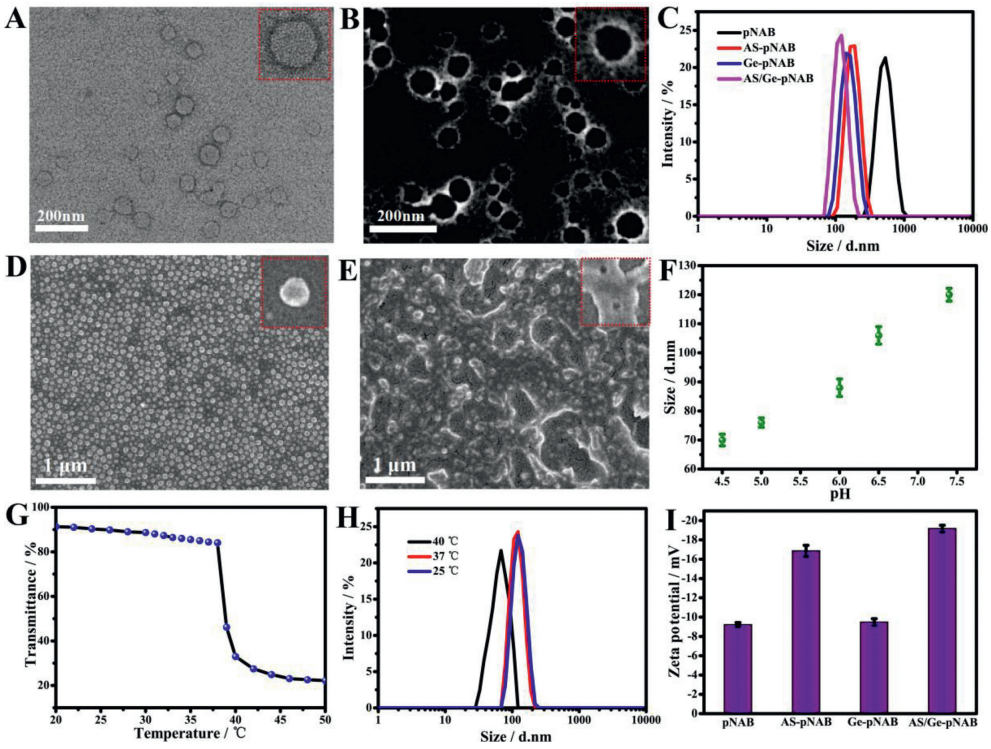

Fig. 1. (A) TEM image of the AS/Ge-pNAB microgels after staining with uranyl acetate. (B) HAADF TEM image of the AS/Ge-pNAB microgels. (C) DLS results of these microgels in 1× PBS (pH 7.4). (D) Scanning electron microscope (SEM) analyses of the AS/Ge-pNAB microgels that were treated with 10 μmol/L (D) or 10 mmol/L GSH (E). (F) DLS analyses of the AS/Ge-pNAB microgels at varying pH levels. (G) The curve of transmittance of the AS/Ge-pNAB microgels as a function of temperature. (H) DLS analyses of the AS/Ge-pNAB microgels at different temperatures. (I) Zeta potentials of these microgels in 1× PBS (pH 7.4). The insets in A, B, D, and E were high-resolution images of a single microgel. Data are presented as mean ± standard deviation (SD) (n = 3).

structures with an outer dark ring which depicted that the microgels AS/Ge-pNAB have double-layer structures with DNA in the outer layer (Fig. 1A). Contrastingly, the untargeted pNAB microgels formed single-layer structures after uranyl acetate staining (Fig. S2 in Supporting information). The typical bilayer morphology of the AS/Ge-pNAB microgels was also confirmed through high-angle annular dark-field (HAADF) TEM imaging followed by staining with uranyl acetate (Fig. 1B). Since studies have shown that heavier elements give brighter contrasts in HAADF, we speculated that the outer layer is richer in uranium than the core, and thus would be richer in DNA. Such structural features will help DNA ligands recognize receptors on the tumor cells. The sizes of the AS/Ge-pNAB microgels and other control microgels were investigated by dynamic light scattering (DLS, Fig. 1C), and the sizes of AS/Ge-pNAB, AS-pNAB, Ge-pNAB, and pNAB microgels were 115, 175, 148, and 502 nm, respectively. This depicted that the modification of targeting ligands is beneficial in terms of reduction of the particle size, and the microgels with appropriate size can be obtained by fluctuating the concentration of ligands.

Subsequently, the triple-responsive properties of the AS/Ge-pNAB microgels were investigated. Upon treatment with 10 μmol/L glutathione (GSH), the AS/Ge-pNAB microgels can maintain uniform spherical morphology (Fig. 1D). In contrast, after treating the AS/Ge-pNAB with 10 mmol/L GSH for 30 min, the microgels were decomposed, collapsed and stuck together (Fig. 1E). This is due to the disruption of the disulfide bond in the cross-linking agent, indicating the microgels have sensitive responsiveness to the tumor reductive environment. Meanwhile, DLS and TEM results showed that the AS/Ge-pNAB size was pH-dependent (Fig. 1F and Fig. S3 in Supporting information). At pH 7.4, the microgels showed osmotic swelling (~115 nm) which can be associated with the electrostatic repulsion between the deprotonated carboxylic groups of acrylic acid (AA). When the environment changes to acidic, the particle size of the microgels decreases gradually due to the protonation of the carboxyl group. The above showed that the microgels had sensitive pH response capability. Furthermore, Fig. 1G showed that the transmittance change of the AS/Ge-pNAB microgels acts as a function of temperature which indicated that the lower critical solution temperature (LCST) was 39 °C, which was just above the normal body temperature. Under the body temperature, the AS/Ge-pNAB was swollen and in a hydrophilic state. Meanwhile, when the temperature was higher than the LCST, it would transform to a shrunken and hydrophobic state rapidly. Fig. 1H shows the sizes of AS/Ge-pNAB at different temperatures. These results indicated that AS/Ge-pNAB had controllable and reversible temperature response. In addition, the surface charge of different microgels was monitored by DLS measurements. All microgels presented negative potential, which would be favorable for long-term circulation to enhance the accumulation of nano drugs in tumors (Fig. 1I). Finally, the stability of AS/Ge-pNAB microgels under simulated physiological condition was investigated (Fig. S4 in Supporting information). These results showed that AS/Ge-pNAB could keep the size and dispersion unchanged for a long time which depicted that the AS/Ge-pNAB microgels had excellent stability.

The GA was encapsulated into microgels through three consecutive cycles of heating and cooling to obtain nano-herb (AS/Ge-pNAB@GA). After the optimization of the loading conditions (Fig. S5 in Supporting information), GA encapsulation efficiency (EE) and loading capacity (LC) values increased to 86% and 25%, respectively. Next, the release of GA from the nano-herb was assessed in phosphate buffer saline (PBS) under a range of conditions (Fig. S6 in Supporting information). The results proved that the AS/Ge-pNAB microgels could provide stable nanostructures for drug entrapment, maintained stability during systematic blood circulation, and could control drug release at tumor sites. The biocompatibility of the various microgels was investigated, and the results demon-

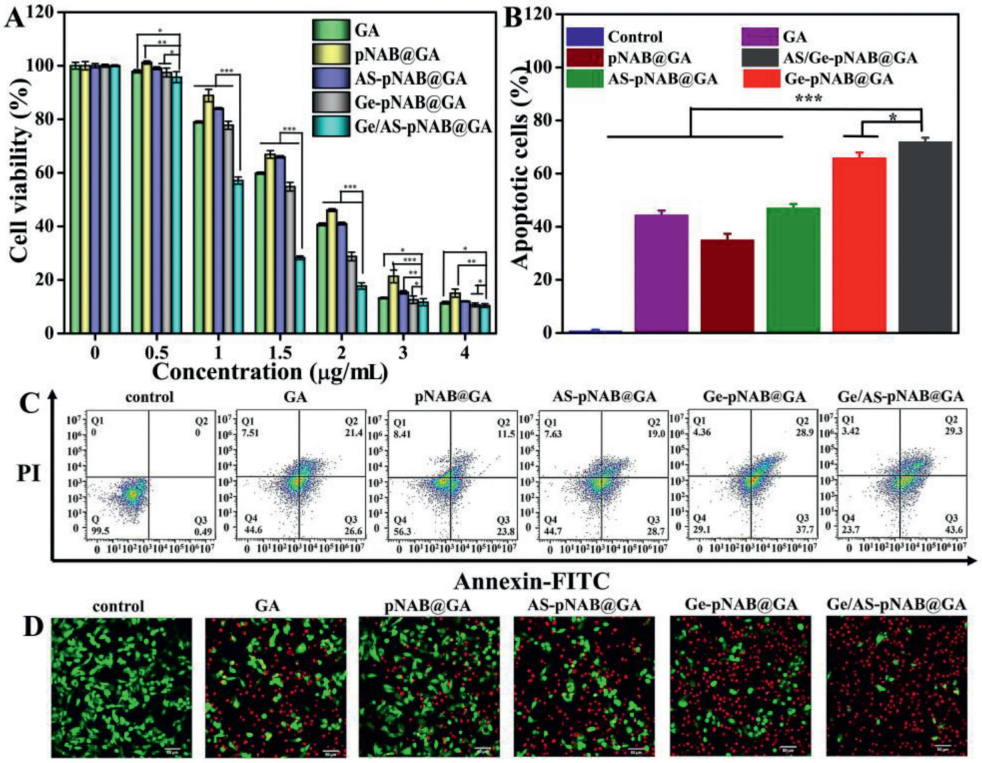

Fig. 2. (A) The cytotoxicity of $HepG_2$ cells exposed to various concentrations of free GA, pNAB@GA, AS-pNAB@GA, Ge-pNAB@GA, and AS/Ge-pNAB@GA (GA dosage: 0, 0.5, 1, 1.5, 2, 3 and 4 μg/mL) for 24 h. (B) Percentage of apoptotic cells including early and late-stage apoptotic cells in different groups. (C) Confocal laser scanning microscope (CLSM) images of live/dead cell staining assay in different groups. (D) The apoptosis of $HepG_2$ cells induced by different groups was analyzed by Annexin V-FITC/PI staining based on flow cytometric. Scale bar: 50 μm. Data are presented as mean ± SD ($n = 3$). $^{*}P < 0.05$, $^{**}P < 0.01$, $^{***}P < 0.001$.

strated that all the microgels had excellent biocompatibility at a wide range of concentrations (Fig. S7 in Supporting information). To evaluate the cellular uptake efficiency, all the microgels were labeled with fluorescein isothiocyanate (FITC) to generate fluorescence signals. The flow cytometric (Fig. S8 in Supporting information) and fluorescence microscope (Fig. S9 in Supporting information) results indicates that the uptake efficiency of targeted modified microgels to $HepG_2$ cells was higher than the non-targeted pNAB microgels. Moreover, the double-targeted AS/Ge-pNAB microgels exhibited the highest uptake efficiency, which can be associated with the receptor-mediated internalization process. Meanwhile, we prepared DNA-templated Ag NCs on the AS/Ge-pNAB microgels, and the obtained hydrophilic AS/Ge-pNAB-Ag NCs have strong red fluorescence (Fig. S10 in Supporting information). The AS/Ge-pNAB-Ag NCs depict the ability to maintain good fluorescence stability for a long time even in high temperature, reductive and acidic environments (Fig. S11 in Supporting information). This provided the possibility of imaging *in vivo*. Moreover, the AS/Ge-pNAB-Ag NCs exhibited little cytotoxicity on $HepG_2$ cells and 3T3 cells at a wide range of concentrations (Fig. S12 in Supporting information), which depicted that the Ag NCs had good biosafety. After incubating the $HepG_2$ cells with AS/Ge-pNAB-Ag NCs for 4 h, the confocal fluorescence images exhibited bright red fluorescence in the nucleus and cytoplasm of the tumor cells (Fig. S8). This demonstrated that the AS/Ge-pNAB-Ag NCs could effectively enter cells and obtain tumor cell-specific imaging based on ligand-receptor recognition, which provided the possibility to dynamically monitor the drug delivery process.

The *in vitro* cytotoxicity of AS/Ge-pNAB@GA against $HepG_2$ cells was evaluated and compared to free GA and controlled GA-loaded microgels using MTT assays. It was found that all treatment groups showed dose-dependent cytotoxicity. The non-targeted pNAB@GA ($IC_{50} = 1.884$ μg/mL) showed lower cytotoxicity than free GA ($IC_{50} = 1.596$ μg/mL), which can be linked to the fact that free GA is more conducive to diffusion than passive targeted pNAB@GA. In contrast, single-targeted AS-pNAB@GA ($IC_{50} = 1.684$ μg/mL) and Ge-pNAB@GA ($IC_{50} = 1.505$ μg/mL) showed enhanced cytotoxicity, which may be ascribed to ligand recognition to promote drug entrance into tumor cells. As per the anticipation, the double-targeted AS/Ge-pNAB@GA ($IC_{50} = 1.246$ μg/mL) induced the strongest cytotoxicity even better than free GA, which may be the result of combined effects of double-targeted recognition promoting cell internalization and increased bioavailability of poorly soluble drugs (Fig. 2A). The *in vitro* antitumor efficacy of the AS/Ge-pNAB@GA against $HepG_2$ cells was also evaluated through Annexin-V-FITC/propidium iodide (PI) apoptosis assay. Figs. 2B and C show that the tumor cells treated with AS/Ge-pNAB@GA depicted the strongest ability to induce apoptosis, and exhibited a very significant difference in total apoptosis ratio with free GA and other three control treatments, which showed conformance with the results of cell viability assay. Meanwhile, ability of GA, and eventually improve the therapeutic applications of GA for cancer treatment.

Based on the excellent antitumor performance *in vitro*, we further investigated the *in vivo* antitumor capability of AS/Ge-pNAB@GA on $HepG_2$ tumor-bearing mice, and compared it with free GA and controlled GA-loaded microgels. The animal care and experiments were performed in accordance with the animal research ethics committee of Tianjin University of Traditional Chinese Medicine. Fig. 3A showed the tumor growth curves of six different treatment groups of mice over a 17-day period. It was found that the tumor growth rates were reduced in all other treatment groups as compared to the normal PBS group. The tumor growth rate was much lower for AS/pNAB@GA, Ge-pNAB@GA, and AS/Ge-pNAB@GA treatment groups as compared to free GA and pNAB@GA groups. Further, the average tumor volume of AS/pNAB@GA, Ge-

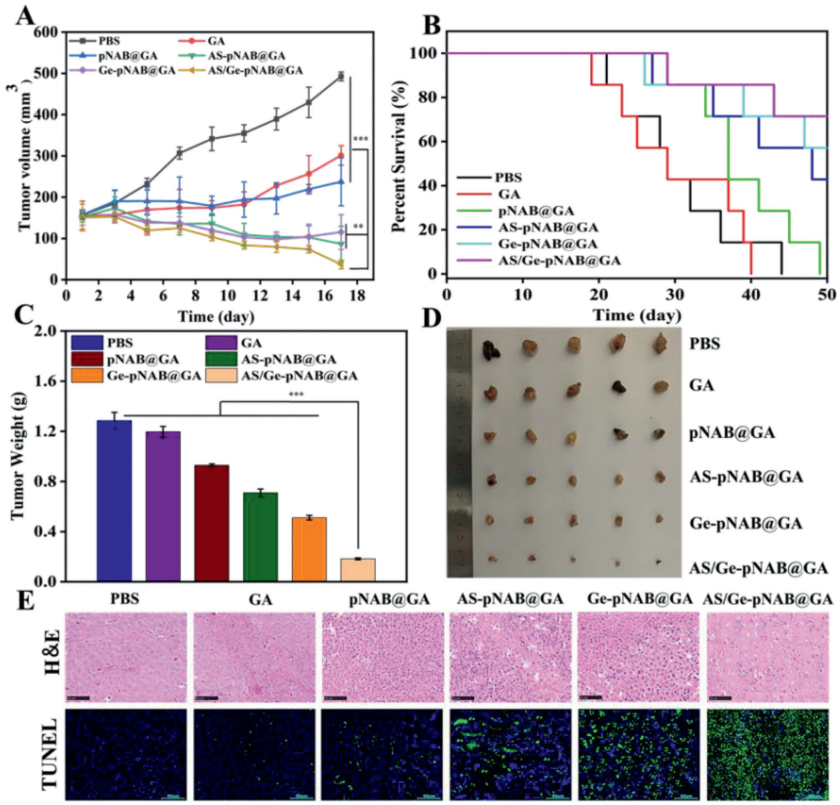

Fig. 3. (A) Tumor growth curves of the mice treated with PBS, GA, pNAB@GA, AS-pNAB@GA, Ge-pNAB@GA, and AS/Ge-pNAB@GA at a dose of 4 mg/kg GA. (B) Survival profiles of $HepG_2$ tumor-bearing mice after treatment with various groups. The weight (C) and photos (D) of tumors peeled from the mice at the therapeutic terminal. (E) H&E staining and TUNEL immunohistochemical staining of the harvested tumor tissues from different groups. Scale bars: 100 μm. Data are presented as mean ± SD ($n = 6$). $^{**}P < 0.01$, $^{***}P < 0.001$.

pNAB@GA, and AS/Ge-pNAB@GA treatment groups on day 17 was 115, 87, and 37 mm^3, respectively, which were significantly smaller than those in the free GA treatment group (301 mm^3). In particular, the AS/Ge-pNAB@GA group showed excellent antitumor performance with a tendency to eliminate the tumor. At *in vivo* experiment end, the tumor tissues were taken out for photographing and weighing. Comparable results were also noticed in Figs. 3C and D, wherein the tumor of AS/Ge-pNAB@GA treatment group was the smallest, and the results were in line with the tumor volume data in Fig. 3A. The harvested tumor tissues were analyzed using hematoxylin-eosin staining (H&E) staining and terminal-deoxynucleotidyl transferase mediated nick end labeling (TUNEL) assay to further validate the antitumor effects. The corresponding results are displayed in Fig. 3E. H&E staining depicted that the tumor cells of the PBS group were dense without observable damage, whereas different extents of tumor cell reduction were observed in the treated groups, characterized by the nuclear and cytosolic degradation. It is important to highlight that the AS/Ge-pNAB@GA-treated group had the most significant increase in cell-free necrosis area compared to other groups. Meanwhile, the apoptosis cells were estimated by TUNEL staining. It showed that the frequencies of apoptotic TUNEL-positive cells increased in the following order: PBS, GA, pNAB@GA, AS-pNAB@GA, Ge-pNAB@GA, and AS/Ge-pNAB@GA. As per our speculation, the AS/Ge-pNAB@GA-treated group showed the highest proportion of apoptotic cells. Meanwhile, the AS/Ge-pNAB@GA-treated mice achieved the longest survival time compared with free GA and the other three control groups (Fig. 3B). This can be due to its most potent antitumor capacity. Taken together, these results were in line with the aforementioned tumor volume and tumor weight which explicitly showed that the AS/Ge-pNAB@GA had a superior antitumor effect. Meanwhile, the microgels can be used for *in vivo* imaging based on the fluorescence of Ag NCs, both *in vivo* imaging and *ex vivo* images results (Fig. S13 in Supporting information) showed that the AS/Ge-pNAB-Ag NCs are more likely to aggregate at the tumor site, this can be explained by the combination of the enhanced permeability and retention (EPR) effect and dual-ligand-mediated internalization.

Toxic effects are a primary barrier in the application of drug therapy *in vivo* which implies that monitoring the systemic toxicity of drugs is pivotal. Therefore, the biosafety of each treatment group was evaluated by body weight change, H&E staining and serum biochemical analysis. The weight of mice in the GA treatment group was relatively stable at first but decreased significantly after the eleventh day which depicted the presence of systemic toxicity in the free drug. However, the weight of mice in other groups (PBS, pNAB@GA, AS-pNAB@GA, Ge-pNAB@GA, and AS/Ge-pNAB@GA) did not show any changes which suggested that these nano formulations had superior biosafety (Fig. 4B). Meanwhile, the H&E staining results showed that the GA treatment group had liver inflammatory damage evidenced by moderate level of inflammatory cell infiltration and cell necrosis, while the main organs in the other treatment groups had no abnormalities or lesions (Fig. 4A). Additionally, the serum enzyme markers concentrations of the heart (creatine kinase (CK)), liver (aspartate transaminase (AST) and aminotransferase (ALT)), and kidney (blood urea nitrogen (BUN) and creatinine (CRE)) were also studied. The results showed that GA increased the levels of AST and ALT which indicates liver toxicity. In contrast, none of these parameters were abnormally altered in mice in any nano formulations treatment groups (Figs. 4C–G) which can be associated with remarkably enhanced tumor accumulation. Together, these results and findings support the ability

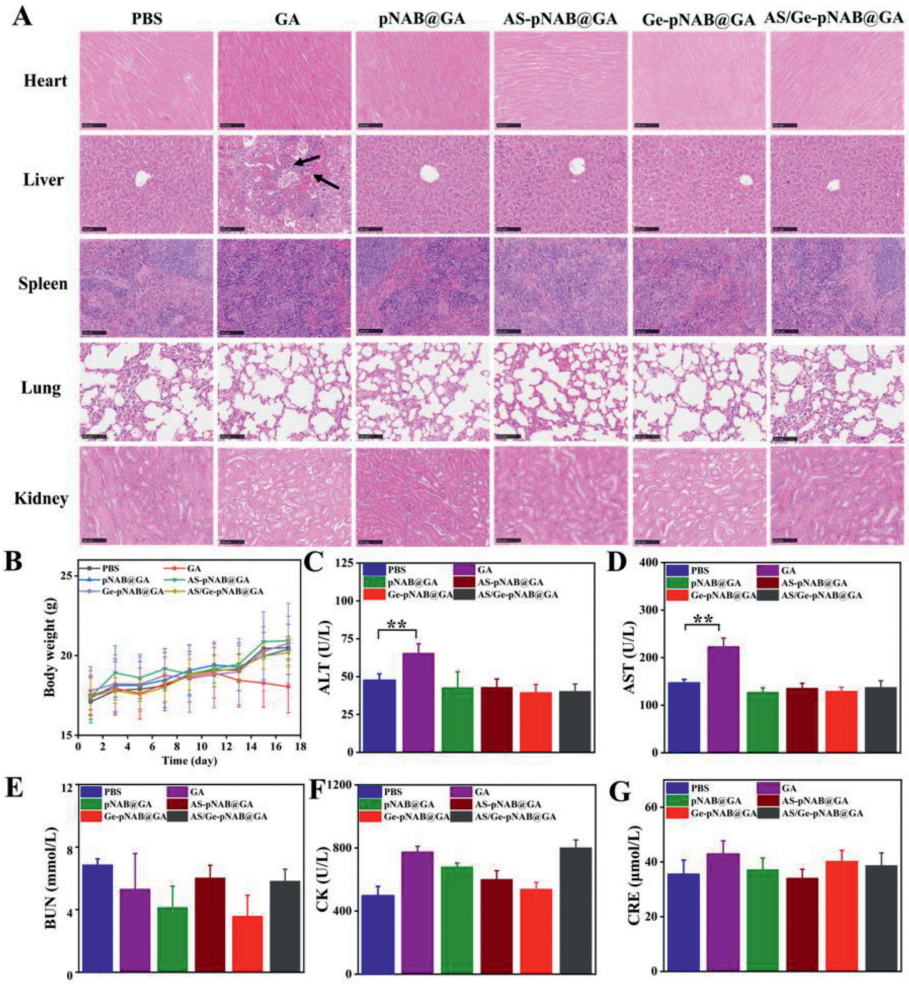

Fig. 4. (A) Histopathological examination of the excised major organs in the indicated treatment groups at the therapeutic terminal. Scale bars: 100 μm. The black arrows indicate the injured site. (B) Variations of body weight in different treatment groups of mice. (C–G) Serum biochemistry data in different treatment groups of mice on day 17. The normal ranges of CK, AST, ALT, BUN, and CRE are 99–1100, 69.5–210.0, 33.0–99.0, 2.00–7.70, and 22.0–97.0, respectively. Data are mean ± SD ($n = 6$). $^{**}P < 0.01$.

of AS/Ge-pNAB@GA to mitigate GA-associated toxicity, highlighting the value of this DDS for use in targeted cancer therapy.

To summarize, in this work, we developed a straightforward approach to synthesize multifunctional microgels which have dual-active targeting, triple environment responsiveness, and fluorescence imaging capability amenable to effective GA delivery. The GA-loaded microgels, also called nano-herb, were highly stable in normal physiological conditions and were able to readily accumulate within tumors to deliver their encapsulated cargo drugs to tumor cells. After uptake by tumor cells, the endosomal acidic pH and intracellular high GSH level triggered the contraction of microgels followed by decomposition which accelerated the drug release for killing cells. Accordingly, the AS/Ge-pNAB@GA treatment had enhanced therapeutic effects *in vitro* and *in vivo* and showed high suppression of target tumor growth. Meanwhile, the biosafety profiles of these multifunctional nano-formulations *in vivo* were also satisfactory, and they were associated with fewer side effects as compared to free GA treatment. Overall, these results indicate that the multifunctional microgels entail the potential and advantages suitable for their use as a GA delivery system in cancer therapy. These microgels have the potential capacity to treat a range of cancer types. To conclude, this reliable and straightforward strategy of building multifunctional drug delivery platforms opens a new avenue for the development of novel antitumor therapeutic delivery systems suitable for clinical deployment.

Declaration of competing interest

The authors declare that they have no known competing financial interests or personal relationships that could have appeared to influence the work reported in this paper.

Acknowledgments

This research was financially supported by the National Natural Science Foundation of China (Nos. 21907076 and 31901908), Natural Science Foundation of Tianjin (No. 22JCQNJC01570) and Scientific Project of Tianjin Municipal Education Commission (No. 2022KJ026). The author Fengyun Li thanks her husband Jingbo Liu and son Yufan Liu for their support in scientific research.

Supplementary materials

Supplementary material associated with this article can be found, in the online version, at doi:10.1016/j.cclet.2023.108752.

References

[1] B.J. Sun, C. Lou, W.P. Cui, et al., J. Control. Release 264 (2017) 145–159.
[2] J.J. Shi, P.W. Kantoff, R. Wooster, et al., Nat. Rev. Cancer 17 (2017) 20–37.
[3] B. Vuong, A. Dehal, A.N. Graff-baker, et al., J. Clin. Oncol. 35 (2017) 233.
[4] J. Guan, W. Chen, M. Yang, et al., Adv. Drug Deliv. Rev. 174 (2021) 210–228.

[5] M. Chen, X. Zhou, R. Chen, et al., Mater. Today 25 (2018) 66–87.
[6] R. Pu, X. Li, L. Zhang, et al., Ann. Oncol. 30 (2019) vi104.
[7] E. Hatami, M. Jaggi, S.C. Chauhan, et al., Acta Rev. Cancer 1874 (2020) 188381.
[8] K. Banik, C. Harsha, D. Bordoloi, et al., Cancer Lett. 416 (2018) 75–86.
[9] G. Bai, P. Yuan, B. Cai, et al., Adv. Funct. Mater. 29 (2019) 1904401.
[10] Y.H. Wang, C.Y. Yue, M.Y. Zhang, et al., Chem. Eng. J. 452 (2022) 139108.
[11] D.S. Ling, H.P. Xia, W. Park, et al., ACS Nano 8 (2014) 8027–8039.
[12] X.Y. Wan, H. Zhong, W. Pan, et al., Angew. Chem. Int. Ed. 58 (2019) 14134–14139.
[13] H.J. Li, W.X. Yan, X.M. Suo, et al., Biomaterials 200 (2019) 1–14.
[14] X.H. Zhou, X.L. He, K. Shi, et al., Adv. Sci. 7 (2020) 2001442.
[15] G. Gao, Y.W. Jiang, Y.X. Guo, et al., Adv. Funct. Mater. 30 (2020) 190939.
[16] L.J. Yang, X.X. Hou, Y.M. Zhang, et al., J. Control. Release 339 (2021) 114–129.
[17] L.F. Han, Y.M. Wang, X.X. Huang, et al., Biomaterials 257 (2020) 120228.
[18] X.M. Su, Y.B. Cao, Y. Liu, et al., Mater. Today Bio 12 (2021) 100154.
[19] H. Park, G. Saravanakumar, J. Kim, et al., Adv. Healthc. Mater. 10 (2021) 2000834.
[20] D. Pe'er, S. Ogawa, O. Elhanani, et al., Cancer Cell 39 (2021) 1015–1017.
[21] B.B. Mendes, D.P. Sousa, J. Conniot, et al., Trends Cancer 7 (2021) 847–862.
[22] G. Petroni, A. Buqué, L.M. Coussens, et al., Nat. Rev. Drug Discov. 21 (2022) 440–462.
[23] G.N. Liu, X. Zhao, Y.L. Zhang, et al., Adv. Mater. 31 (2019) 1900795.
[24] Z. Lv, M. Huang, P. Li, et al., Chin. Chem. Lett. 34 (2023) 108601.
[25] B. Lin, H. Su, R. Jin, et al., Sci. Bull. 60 (2015) 1272–1280.
[26] B. Park, S. Park, J. Kim, et al., Adv. Drug Deliv. Rev. 184 (2022) 114235.
[27] C. Cheng, Y. Gao, W.H. Song, et al., Chem. Eng. J. 380 (2020) 122474.
[28] J. Sun, J. Li, X. Li, et al., Chin. Chem. Lett. 34 (2023) 107891.
[29] Q. Wu, C.C. Liu, Y. Liu, et al., ACS Appl. Mater. Interfaces 14 (2022) 14953–14960.
[30] X. Yan, Y. Qi, L. Ren, et al., J. Control. Release 348 (2022) 470–482.
[31] F.A. Plamper, W. Richtering, Acc. Chem. Res. 50 (2017) 131–140.
[32] F. Li, D. Lyu, S. Liu, et al., Adv. Mater. 32 (2019) 1806538.
[33] Y.T. Wang, L.X. Guo, S.L. Dong, et al., Adv. Colloid Interface Sci. 266 (2019) 1–20.
[34] M. Molina, M. Asadian-Birjand, J. Balach, et al., Chem. Soc. Rev. 44 (2015) 6161–6186.
[35] D.J. McClements, Adv. Colloid Interface Sci. 240 (2017) 31–59.